PAPER • OPEN ACCESS

CFD and FEM analysis to migrate from fixed- to variable-speed on the Alto Lindoso HPP

To cite this article: Olivier Pacot *et al* 2022 *IOP Conf. Ser.: Earth Environ. Sci.* **1079** 012069

View the article online for updates and enhancements.

CFD and FEM analysis to migrate from fixed- to variable-speed on the Alto Lindoso HPP

Olivier Pacot[1], Joachim Delannoy[3], François André[3], Claire Segoufin[3], João Delgado[4], Miguel Roque[5], Cécile Münch-Alligné[1,2]

[1] Institute of Sustainable Energy, School of Engineering, University of Applied Sciences and Arts Western Switzerland Valais, Sion, Switzerland

[2] Institute of Systems Engineering, School of Engineering, University of Applied Sciences and Arts Western Switzerland Valais, Sion, Switzerland

[3] GE Renewable Energy, Hydro Solutions, 82 Avenue Léon Blum, 38041 Grenoble Cedex 9, France

[4] EDP NEW R&D – Centre for New Energy Technologies, Rua Cidade de Goa 4, 2685–039 Sacavém, Portugal

[5] EDP Produção, Rua Ofélia Diogo Costa 45, 4100-482 Porto, Portugal

olivier.pacot@hevs.ch

Abstract. The need to decarbonise our energy system push us toward the use of different clean renewable energy sources, such as solar, wind and hydroelectric energy. It is well known that some of these renewable energy sources suffer of intermittence, which requires the conventional dispatchable power plants to become more flexible to respond to any power change to ensure a stable electrical grid. For this specific purpose, the European project XFLEX HYDRO is focusing on the hydropower sector, with seven demonstrators in three different countries to demonstrate the possibility to enhance the flexibility, one option being to use the variable-speed technology combined with smart digital control. Among these seven demonstrators, one is the Alto Lindoso hydropower plant owned by EDP and located in North-West of Portugal. It consists of two fixed-speed vertical Francis turbines with a high head of approximately 275 m and a rated power of 317 MW. The objective of this demonstrator is to assess the potential of a variable speed using the Doubly Fed Induction Machine (DFIM) technology to increase the flexibility of the power and the lifetime of the turbine. Therefore, this paper explores numerically the hydraulic behaviour of the model runner when operated at a selected part load conditions (60% BEP) with the rotational speed changed by ±10%. Second, a FEM analysis is carried out to evaluate the runner blades damage rate. This preliminary study showed that in term of wear and tear, the variable speed technology would bring in an advantage.

1. Introduction
The pressure on governments is continuously growing to change their policy to reduce or even cancel their dependency on fossil fuel. This means that renewable energies, such as solar and wind, need to

massively penetrate the market. However, this is not sufficient as an additional solution must be implemented to respond to the intermittency of these energies and to be able to store the surplus of energy. Hydropower plants (HPP) can play a key role in this solution as they can quickly respond to any demand change and, they can act as a massive battery by pumping water in higher reservoirs when the demand is lower than the offer. Nevertheless, using powerplant designed and built several decades ago when their usage was completely different is not straightforward. For example, it was shown that transient behaviour can impact the hydraulic turbine [1][2] as well as the components of the powerplant [3][4]. Reviews on the efforts put on to understand the physics and to estimate the fatigue life can be found in [5], [6]. In that context, the European project XFLEX HYDRO [7] aims to develop a Smart Power Plant Supervisor (SPPS) to extend the flexibility of the power system and simultaneously to minimise the damage resulting from this required flexibility. This supervisor will have an accurate knowledge of each component within a powerplant allowing it to dispatch the requested power to minimise the powerplant wear and tear.

The present study focusses on the demonstrator Alto Lindoso and follow on from the study performed on Caniçada [8] to assess the advantage of the variable speed technology. For this study, CFD and FEM computations were performed and are presented, respectively, in sections 4.1. and 4.2. .

2. Case Study
The case study is the Alto Lindoso HPP, whose layout is shown in Figure 1. This HPP is equipped with two vertical Francis turbines of 317 MW powered with a nominal head of 276 m and a discharge of 125 m3/s. The distributor is composed of 20 guide vanes and the runner of 13 blades. The numerical simulations were, however, performed at the model scale with a diameter of 0.33 m and a head of 20 m.
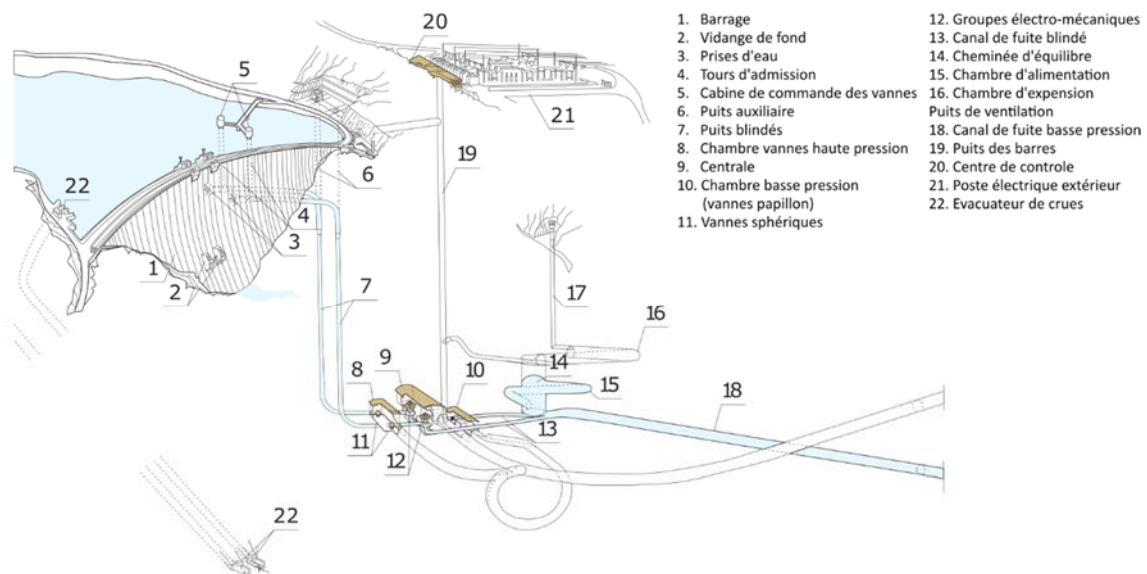

1. Barrage
2. Vidange de fond
3. Prises d'eau
4. Tours d'admission
5. Cabine de commande des vannes
6. Puits auxiliaire
7. Puits blindés
8. Chambre vannes haute pression
9. Centrale
10. Chambre basse pression (vannes papillon)
11. Vannes sphériques
12. Groupes électro-mécaniques
13. Canal de fuite blindé
14. Cheminée d'équilibre
15. Chambre d'alimentation
16. Chambre d'expension
Puits de ventilation
18. Canal de fuite basse pression
19. Puits des barres
20. Centre de controle
21. Poste électrique extérieur
22. Evacuateur de crues

Figure 1: Alto Lindoso HPP layout [9].

3. Methodology

3.1. Selection of a specific part load operating point
To evaluate if variable speed can mitigate the aging of the runner, the operating point, where the maximum radial forces are exerted on the runner, was selected. This operating point was obtained by carrying several CFD computations at the synchronous speed ($n_{11} = 48$ min^{-1}) while changing the guide vane opening. It resulted that the part load condition at 60% ($Q_{11} = 269$ l/s) of the best efficiency point

is roughly responsible for the highest radial forces, see Figure 2 (right). From there, the runner speed was changed by ±10%, as if a DFIM converter would be available, and maintaining the output power constant, see Figure 2 (tight).
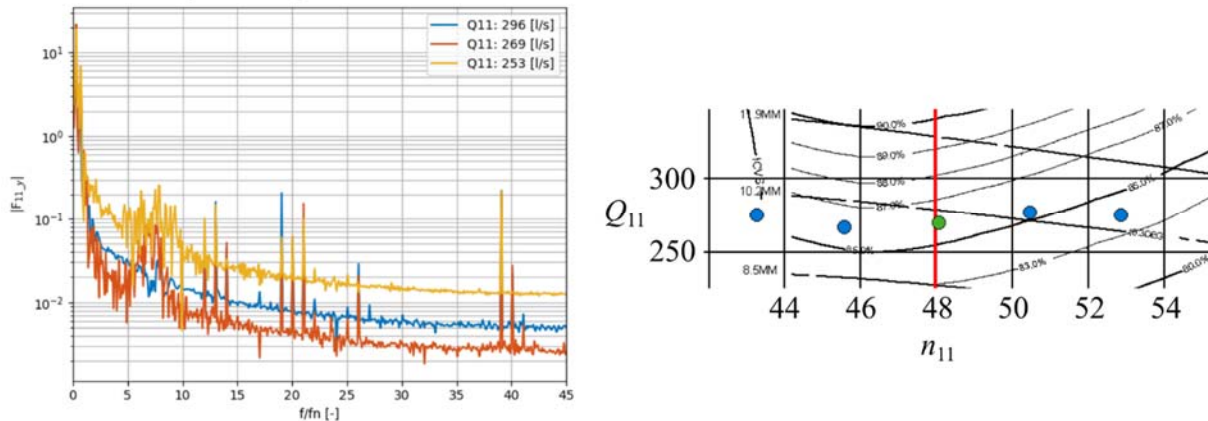

Figure 2: (left) FFT of the radial force F11 acting in the y direction (perpendicular to the inlet and outlet directions) for three part-load operating conditions (stationary frame of reference). (right) Computed operating points.

3.2. CFD setup

The numerical investigation was carried out using the entire runner geometry, i.e., including the spiral casing, the stay and guide vanes, the runner, and the draft tube, see Figure 3. The total mesh is composed of approximately 14 million of elements and was designed using ANSYS ICEM CFD 19R2. To perform the unsteady computations, ANSYS CFX was used, with the k-ω SST turbulence model. The time step size and the RMS residual were set to one degree of revolution and 10^{-5} (four to five inner loops were required for the solution to reach the residual target), respectively. Pressure boundary conditions were applied at the inlet and the outlet of the computational domain to impose a net head.
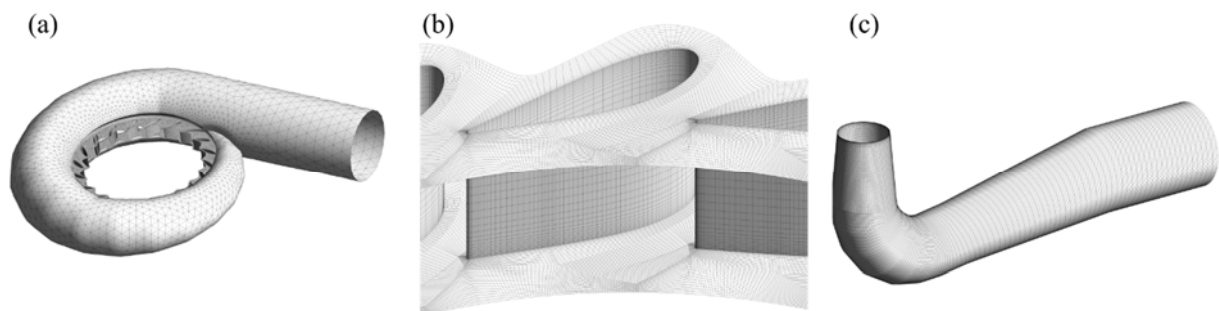

Figure 3: Illustration of the mesh used for the computations: (a) spiral casing (b) distributor and (c) draft tube.

3.3. FEM Setup

The static and transient FEM numerical analysis were carried out using the ANSYS Workbench 2021R2 and considered only the runner. The solid mesh was composed of approximately 2.5 million nodes and 1.6 million quadratic elements and is shown in Figure 4. The element type selected was the quadratic element SURF154, allowing a displacement of the nodes in all three directions. The fixed support was imposed at the shaft and the pressure fields imported from the CFD computations were imposed on the surface. For the transient simulations, the same timestep as the CFD was used, but the data were saved

every two iterations, i.e., every 2° of rotation. The model runner was cast with an aluminium allow AlSi10Mg with the following properties: the density $\rho = 2'670$ [kg m^{-3}], the Young's modulus $E = 76.6$ [GPa], the Poisson's ratio $\nu = 0.33$ [-] and the tensile strength $R_m = 300$ [MPa].
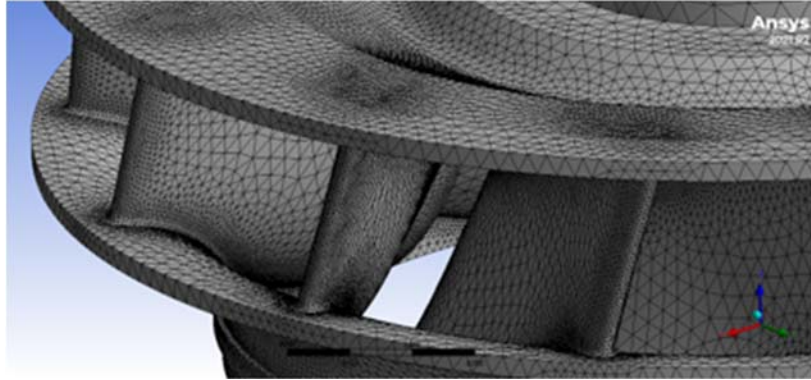

Figure 4: Mesh used for the FEM analysis.

3.4. Damage rate estimation

The computation of the damage rate is following the approach presented in [10]. However, for the completeness of this paper this approach is recalled here. To compare the stress applied on the runner when changing the runner speed, the von-Mises stress is used. From the obtained signal, the rainflow counting algorithm is used, allowing to extract the number of fatigue cycles with their corresponding range and mean. To consider the influence of the mean stress value, the mean stress correction according to Goodman is applied:

$$\Delta\sigma = \sigma_e \frac{R_m - \sigma_m}{R_m} \tag{1}$$

Where σ_e is the fatigue limit and was approximated as $0.45R_m$ [11]. σ_m is the mean stress obtained from the rainflow counting. R_m is the tensile strength of the material. Following the Palmgren-Miner's rule [12], the damage tally D_p is defined as follow for the simulated operating condition p:

$$D_p = \sum_{i=1}^{I} D_{p,i} = \sum_{i=1}^{I} \frac{n_{p,i}}{C\Delta\sigma_{p,i}^{-3}} \tag{2}$$

With $D_{p,i}$ is the damage index, $n_{p,i}$ the number of cycles with a corrected stress range $\Delta\sigma$ and C is a constant depending on the quality category S-N curve [13]. However, as the damage tally is used to compare the impact of different operating conditions, this constant C is cancelled out. Finally, to take into account that the runner is not rotating at the same speed, a damage rate is computed:

$$\dot{D_p} = \frac{D_p}{\Delta t_p} \tag{3}$$

Where Δt_p corresponds to the simulated duration.

4. Results

4.1. CFD

The details of the computed variable speed operating points are shown in Table 1. The variable speed did not bring in any improvement in term of efficiency. Indeed, the maximum is the one obtained at the synchronous speed. The efficiency just decreased slightly when changing the runner speed by ±5%. However, to reach the proper output power has been a challenging task as a change of ±0.01° had sometimes quite an impact on the solution. In term of discharge, there is no advantage as well as all computed points have a discharge higher than the one at the synchronous speed. Since the case at -5%

had an output power less than the expected one, the actual guide vane opening should be increased and, therefore, release more water than the one presented in Table 1.

Table 1: Computed operating points to evaluate the advantage of the variable speed technology. γ represents the guide vane opening and P the output power. The subscript 60% is used to refer to the operating conditions at 60% of the BEP at the synchronous speed. The subscript ss refer to synchronous speed.

n_{11} [min^{-1}]	43.3	45.6	48.1	50.5	52.9
n_{11} / n_{11_ss}	0.90	0.95	1.00	1.05	1.10
$\gamma/\gamma_{60\%}$	0.95	0.94	1.00	1.00	1.02
$P/P_{60\%}$	1.00	0.99	1.00	1.02	1.00
Q_{11} [l/s]	274	266	269	276	274
η [%]	89.4	90.3	90.8	90.5	89.3

The shape of the vortex rope for the different variable speed conditions is shown in Figure 5, using the Q criterion to draw an isosurface. In addition, a normalised pressure contour taken at the location shown by the dashed line is shown. The reference pressure is taken as $p_{ref} = \rho gH$. As it can be seen, the vortex rope does not exhibit anymore a clear spiral shape but is composed of several smaller structures with varying intensity showed by the pressure contours.
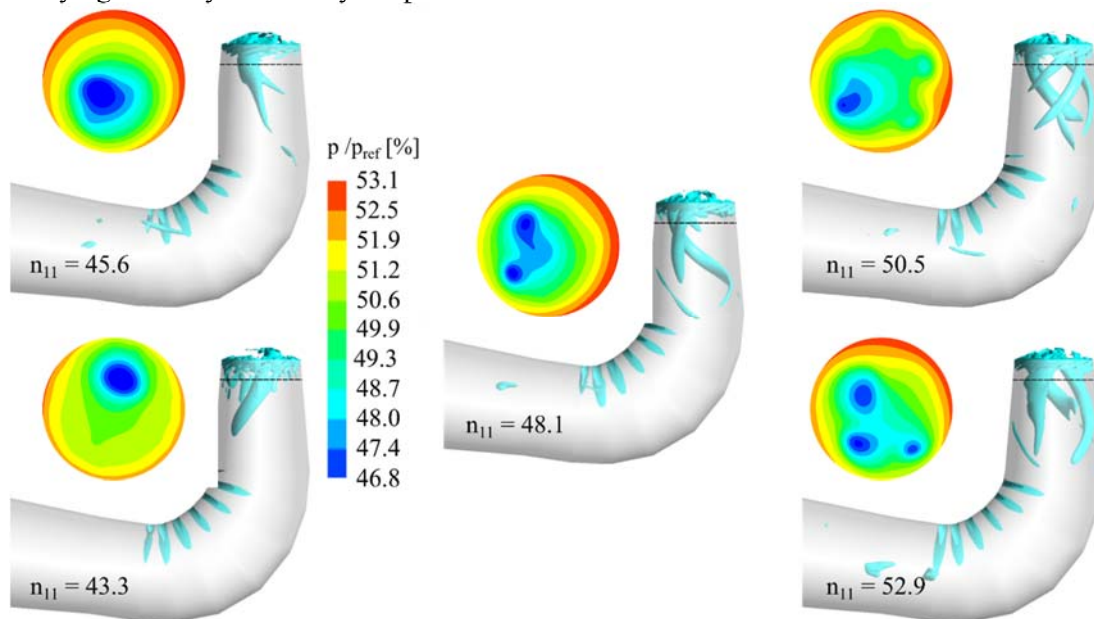

Figure 5: Vortex rope shape using the Q criterion (2000 [s^{-2}]). The dash line shows where is taken the normalised pressure, i.e., $p_{ref} = \rho gH$.

The influence of these vortex ropes on the runner shaft is shown in Figure 6 by the FFT of the normalised forces. In all cases, the highest fluctuation is reached at the frequency of the vortex rope, i.e., $f/f_n = 0.25$. The highest value is reached at the synchronous speed, while the smallest amplitude is reached when lowering the velocity by 10%. The main difference in the spectra is the signature at and around $f/f_n = 13$. It appeared that two vortices are generated at the trailing edge of the guide vanes near the distributor walls. Also, lowering the runner speed induced an increased incident angle of the flow approaching the blade leading edge. As shown in Figure 7, several vortices are seen at lower runner

speed at the blade leading edge and withing the runner passage. Some of these vortices maintains even until some distance after the blade trailing edge.
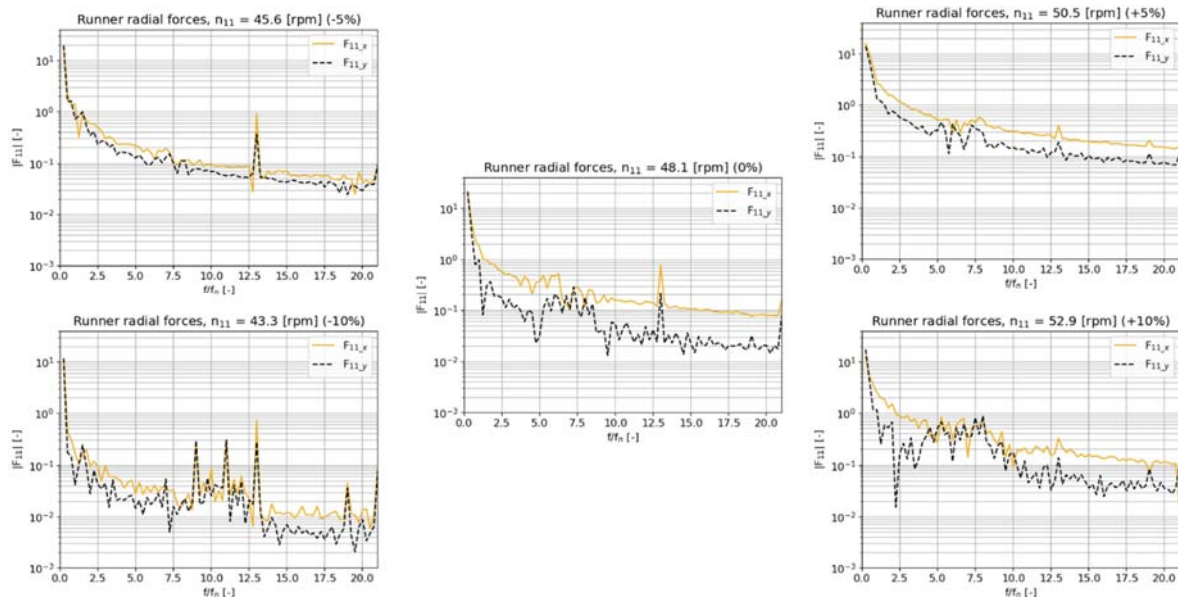

Figure 6: FFT of the radial forces acting on the runner (stationary frame of reference).
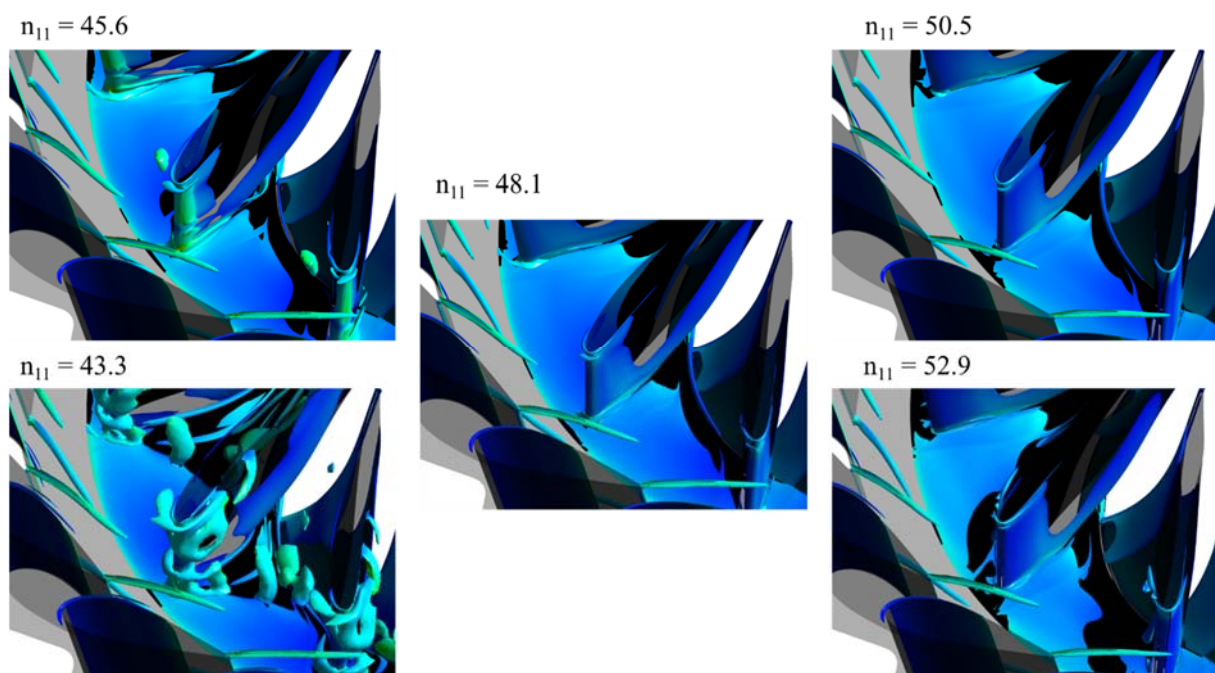

Figure 7: Vortical structures in the distributor and the runner coloured by the turbulent kinematic energy.

Finally, the standard deviation of the normalised pressure is shown in Figure 8 for the different operating conditions. Except for the lowest and highest runner speeds, the main fluctuations take place on the blade leading edge near the suction side because of the rotor stator interaction. For the lowest runner speed, a quite different pattern can be seen. As mentioned previously, the flow field for this specific operating point is affected by upstream vortices generated on the trailing edge of the guide

31st IAHR Symposium on Hydraulic Machinery and Systems

IOP Conf. Series: Earth and Environmental Science   1079 (2022) 012069

IOP Publishing

doi:10.1088/1755-1315/1079/1/012069

vanes. In the runner passage, vortices attached to the suction side near the hub and the leading edge can be seen. These vortices propagate toward the centre of the passage and move toward the shroud, before being forced to rotate and to follow the path at the junction of the blade pressure side and the shroud. For the highest runner speed, the situation is more critical as the fluctuations take place at the trailing edge. Knowing that this part of the blade is the thinner, this operating condition might be more problematic.
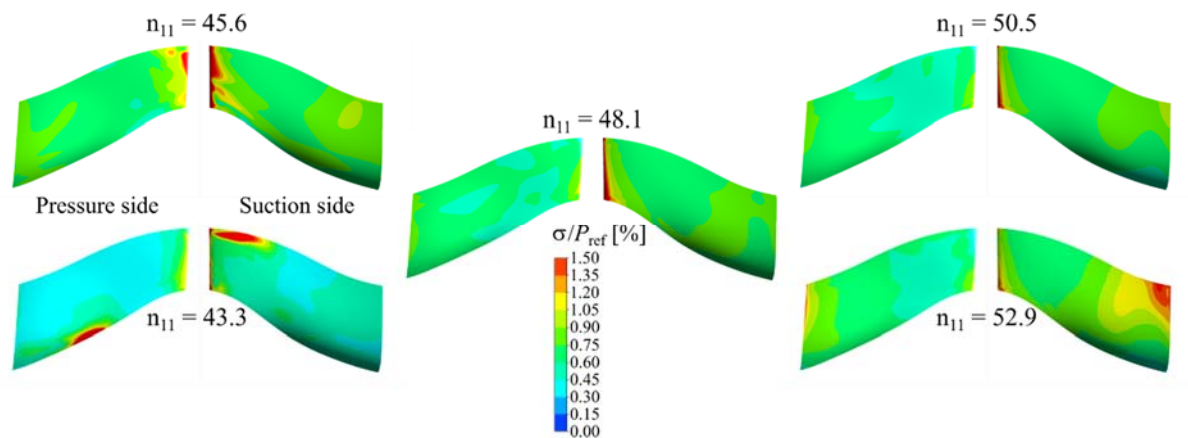

Figure 8: Pressure standard deviation on the blade pressure and suction sides normalised by the reference pressure.

4.2. FEM

A static analysis was first performed to evaluate where the highest stress is applied on the runner at the synchronous speed, $n_{11} = 48.1$ min^{-1}. The maximal equivalent von-Mises stress is located at the trailing edge near the hub pressure side, see Figure 9 a).

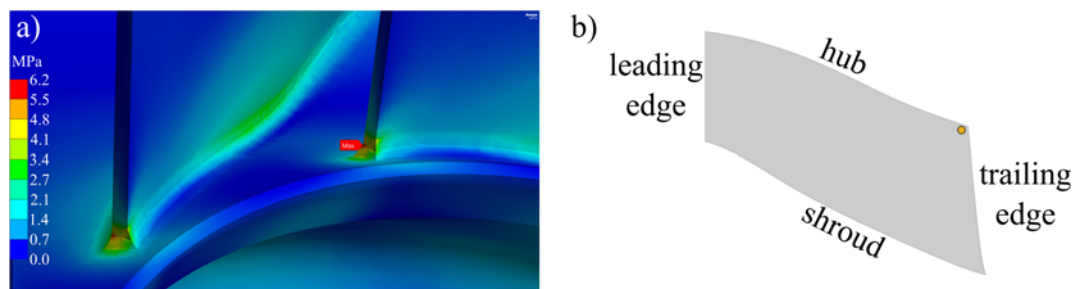Figure 9: a) Static equivalent (von-Mises) stress showing the hotspot. $P/P_{opt} = 60$ %, $n_{11} = 48.1$. b) Location of the monitoring point close to the hotspot on the pressure side.

In addition to the static analysis, a transient quasi-static analysis was performed, and the mean torques T_{11} computed by CFD, and FEM are shown in Table 2 for each different runner speed. The results showed a good agreement between the two approaches. However, the FEM torque always slightly overestimated the CFD value. One explanation is that the viscous effect was included in the computation of the CFD torque. Whereas, in the FEM approach, only the pressure field was imported, and the viscous force considered negligible.

Table 2 : Comparison of the computed T_{11} by CFD and FEM. The torque was averaged during four runner revolutions. The last row shows the relative difference taking the CFD value as reference. The subscript ss refers to synchronous speed.

n_{11} = 43.3 [min^{-1}]		n_{11} = 45.6 [min^{-1}]		n_{11} = 48.1 [min^{-1}]		n_{11} = 50.5 [min^{-1}]		n_{11} = 52.9 [min^{-1}]	
90% n_{11_ss}		95% n_{11_ss}		100% n_{11_ss}		105% n_{11_ss}		110% n_{11_ss}	
CFD	FEM	CFD	FEM	CFD	FEM	CFD	FEM	CFD	FEM
53.9	54.2	50.1	49.9	48.4	48.5	47.0	47.3	44.0	44.5
0.70%		-0.46%		0.10%		0.57%		1.28%	

To monitor the von-Mises stress close to the hotspot, see Figure 9 a), a monitor point, see Figure 9 b), was set in the vicinity of the trailing edge and the hub on the blade pressure side. The normalised stress spectra computed for each runner speed is shown in Figure 10. At this location, the stresses are applying a tension to the structure. For better visibility, the left figure shows the comparison when lowering the runner speed, whereas the right figure shows the comparison when increasing the runner speed with regards to the synchronous speed (n_{11} = 48.1 min^{-1}). As expected, two main peaks can be seen for all runner speeds. The main peak appearing at low relative frequency is the frequency of the vortex rope seen by the runner. This frequency is better seen on the smaller figures showing the spectra in the range f/f_n = [0, 2]. The second peak at f/f_n = 20 is the interaction of one blade with the upstream guide vanes as the signal is taken in the rotating frame of reference. When lowering the runner speed, the two main peaks does not change significantly. However, when lowering the runner speed by 10%, a clear peak at f/f_n = 10 can be seen. At this stage, the reason is not identified. Despite this difference, the trend among the curves is the same. This is not the case when comparing the spectra for the conditions where the runner speed was increased. The two main peaks are present, but for the runner speed increased by 10%, the level of fluctuation among the range f/f_n = [0, 20] is higher, as already observed in Figure 8.
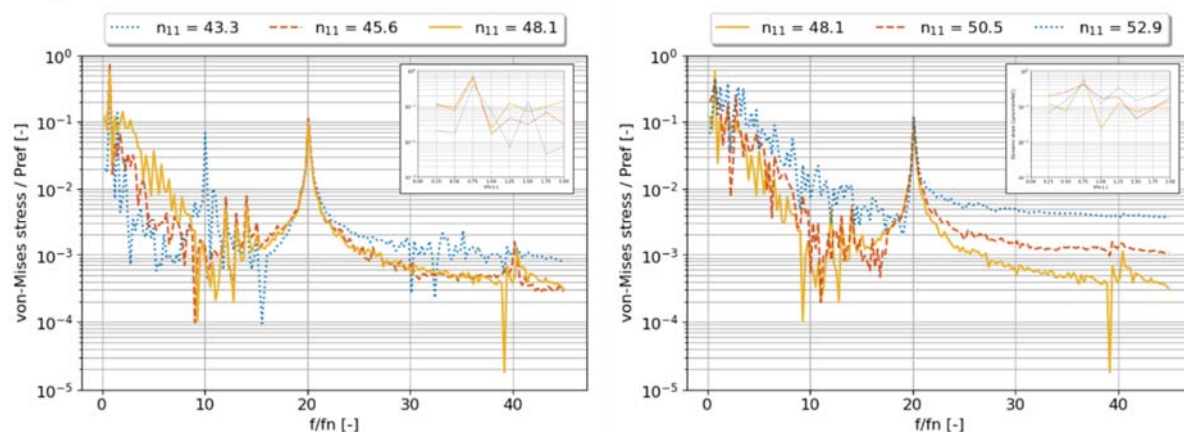

Figure 10: Normalised FFT of the von-Mises stress at the monitoring point shown in Figure 9 b) (rotating frame of reference). (left) comparison when lowering the runner speed. (right) comparison when increasing the runner speed.

Following the procedure introduced in section 3.4. , the relative damage rates, with regards to the one obtained at the synchronous speed, are shown in Figure 11. There is a maximal damage rate operating condition along the constant output power line located around n_{11} = +5%. It can be observed that increasing further the runner speed induced a decrease of the damage rate to reach a level similar to the one when lowering the runner speed by 10%. Therefore, as a first evaluation of the advantage of the variable speed technology, it can be concluded that for this specific operating condition studied, there is an advantage of the variable speed in term of wear and tear. However, this study must be performed for

other operating conditions to assess if the benefit of the variable technology will equal or surpass the cost of this technology and the lower efficiency because of the power electronics.
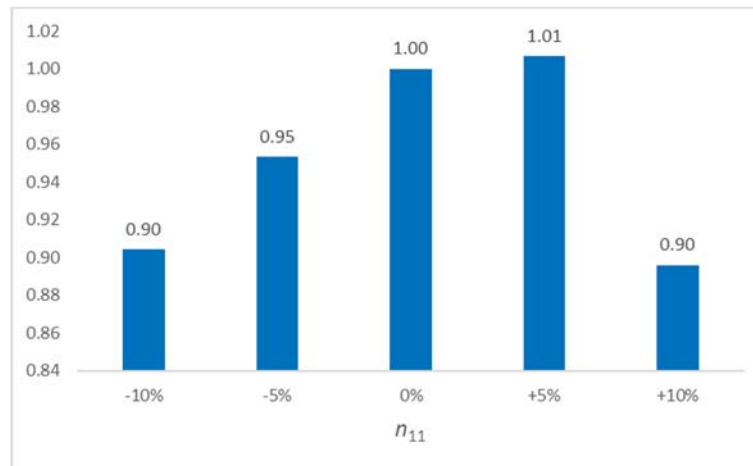

Figure 11: Effect of the runner speed on the damage rate. The damage rate obtained at the synchronous speed is taken as reference.

5. Conclusion

In the framework of the XFLEX HYDRO European project, an analysis to switch from a fixed speed to a variable speed was studied using the Alto Lindoso HPP demonstrator. The usage of a variable speed runner allows to use the machine in the most suited operating condition and the start and stop sequences can be optimised. Therefore, the wear and tear are mitigated. However, to install a variable speed converter requires more civil engineering work and the benefit should equal or surpass an additional loss of about 1.5% because of the power electronic.

To assess the advantage of the variable speed, a CFD analysis was performed using ANSYS CFX with the k-ω SST turbulence model. The selected operating condition is the one imposing the highest radial force on the runner. For this turbine, this condition was reached at 60% of the best efficiency point. From there, the runner speed was changed by ± 10 % to mimic the usage of a DFIM converter. In addition to the runner speed modification, the guide vane opening was duly set to maintain the output power constant. The results showed that the vortex rope was present in all operating condition computed and its impact on the runner radial forces rather constant. However, the study of the pressure fluctuations showed that at the synchronous speed and at ± 5% the main fluctuation appeared on the blade leading edge because of the rotor stator interaction. For the other cases, however, the situation is quite different. The flow within the runner passage is too disturbed and induced pressure fluctuation at different zone. The most problematic condition is when increasing the runner speed by 10% because the zone of high pressure fluctuation appeared near the trailing edge and the hub on the suction side. As this part of the blade is the thinnest, it would be more prone to damage.

The second part of the analysis was dedicated to the structure by performing a FEM analysis using the ANSYS Workbench. First, a static analysis confirmed that the hotspot is located for all cases at the trailing edge near the hub on the blade suction side. Second, a transient quasi-static analysis was performed and the von-Mises stress close to the hotspot was monitored. To compare the result and assess which operating condition is the most suitable, a relative damage rate comparison was performed taking the damage rate at the synchronous speed as reference. This result showed that having a variable speed could be an advantage as the damage rate was approximately 10% lower than the one at the synchronous speed when either increasing or lowering the runner speed by 10%. The maximum damage rate, when moving along the constant output power line, is located around a runner speed increased by 5%.

Finally, this analysis showed that for a specific operating condition, that is, the one exerting the higher radial force on the runner, could benefit from the variable speed technology in term of wear and tear mitigation. However, the efficiency when lowering the runner speed by 10% is more than 1% less than the one at the synchronous speed. Therefore, an additional analysis should be performed to assess the benefit on repair and maintenance versus the loss because of the lower efficiency. Also, this study focused on a single operating condition and a single net head. Further analysis should be performed to evaluate how the variable speed technology would benefit this HPP in other conditions.

Acknowledgments

References
[1]   Trivedi, Chirag, Bhupendra Gandhi, and Cervantes J. Michel. "Effect of transients on Francis turbine runner life: a review." Journal of Hydraulic Research 51.2 (2013): 121-132. DOI:10.1080/00221686.2012.732971

[2]   Gagnon, M., et al. "A look at Francis runner blades response during transients." IOP Conference Series: Earth and Environmental Science. Vol. 49. No. 5. IOP Publishing, 2016. DOI:10.1088/1755-1315/49/5/052005

[3]   C. Nicolet, R. Berthod, N. Ruchonnet, and F. Avellan, "Evaluation of possible penstock fatigue resulting from secondary control for the grid", Proceedings of HYDRO, 2010

[4]   M. Dreyer, C. Nicolet, A. Gaspoz, D. Biner, S. Rey-Mermet, C. Saillen, and B. Boulicaut, "Digital clone for penstock fatigue monitoring," in IOP Conference Series: Earth and Environmental Science, Vol. 405, No. 1. IOP Publishing, 2019. DOI:10.1088/1755-1315

[5]   Trivedi, Chirag, and Michel J. Cervantes. "Fluid-structure interactions in Francis turbines: A perspective review." Renewable and Sustainable Energy Reviews 68 (2017): 87-101. DOI: 10.1016/j.rser.2016.09.121

[6]   Presas, Alexandre, et al. "Fatigue life estimation of Francis turbines based on experimental strain measurements: Review of the actual data and future trends." Renewable and Sustainable Energy Reviews 102 (2019): 96-110. DOI: 10.1016/j.rser.2018.12.001

[7]   International Hydropower Association. (September 2019). XFLEX HYDRO. Retrieved from https://xflexhydro.net/

[8]   Pacot, O., De Colombel, T., Segoufin, C., Delannoy, J., Leguizamon, S., Delgado, J., Roque, M., and Münch-Alligné, C. (2021). "Effect of the variable speed on the hydraulic behavior of the Caniçada Francis turbine". In: SimHydro 2021: Models for complex and global water issues - Practices and expectations, accepted for publication.

[9]   EDP (2016). Declaração Ambiental 2016. Aproveitamentos Hidroelétricos da EDP Produção

[10]   Biner, D., et al. "Turbine mode start-up simulation of a variable speed Francis pump-turbine prototype–Part II: 3-D unsteady CFD and FEM." IOP Conference Series: Earth and Environmental Science. Vol. 774. No. 1. IOP Publishing, 2021. DOI: http://dx.doi.org/10.1088/1755-1315/774/1/012070

[11]   Rodopoulos, C. A. "Safety Factor and Fatigue Life Estimates." Problems of Fracture Mechanics and Fatigue. Springer, Dordrecht, 2003. 491-494.

[12]   A. Nussbaumer, L. Borges, L. Davaine, Fatigue Design of Steel and Composite Structures: Eurocode 3: Design of Steel Structures, Part 1-9 Fatigue, John Wiley & Sons, 2012. DOI:10.1002/9783433608791

[13]   BSI, BS 7910:2013+A1:2015 - Guide to Methods for Assessing the Acceptability of Flaws in Metallic Structures, BSI, 2013.